ORIGINAL ARTICLE

Wear phenomena of grinding wheels with sol–gel alumina abrasive grains and glass–ceramic vitrified bond during internal cylindrical traverse grinding of 100Cr6 steel

Krzysztof Nadolny

Abstract This article presents the results from a traverse internal cylindrical grinding process conducted using grinding wheels with sol–gel alumina abrasive grains and varying volumes of glass–ceramic vitrified bond. The aim was to determine how changing the bond volume within the range of V_b=11.5–14.5 % influenced the wear phenomenon of the microcrystalline sintered corundum abrasive grains and the ceramic bond bridges with glass-crystalline structure. The paper presents grinding wheels with conic chamfer and the most important wear phenomena of the grinding wheel components occurring in the area of contact between the tool and the workpiece material. The work includes the methodology of the experimental tests on the traverse internal cylindrical grinding of bearing rings made from steel 100Cr6 (62±2 HRC). A wide range of test results were analyzed, including machined surface roughness parameters (Ra, Rz, Sm, Δa), grinding power, grinding wheel volumetric wear V_s, material removal V_w, G-ratio, root-mean–square roundness deviation from mean circle (Δ, rms), grinding wheel edge wear, grinding wheel microtopography parameters (Sa, St, Sdr, Sds), and SEM images of the wear marks on the grinding wheel active surface. The dominant wear phenomena of the grinding wheels with conic chamfer and the influence of the bond volume share on its intensity were experimentally determined. The results show that the decrease in bond volume from V_b=14.5 to 11.5 % increases the grinding wheel life by twofold. This was due to a decrease in abrasive wear and plastic flow phenomena and to a greater fracture wear (mostly fatigue and thermal-fatigue). These events led to a periodic shedding of the oxide layer and the plastically deformed grain layer and also revealed the crystals' sharp edges, located below the plastically deformed surface layer.

Nomenclature

CBN	Cubic boron nitride
CPCG	Continuous path-controlled grinding
EDS	Energy-dispersive X-ray spectroscopy
GWAS	Grinding wheel active surface
SEM	Scanning electron microscope
a_e	Working engagement (machining allowance), mm
a_d	Dressing allowance, mm
b	Conic chamfer width, mm
b_w	Workpiece width, mm
d_w	Workpiece diameter, mm
d_s	Grinding wheel outer diameter, mm
G	G-ratio, mm³/mm³
H	Grinding wheel inner diameter, mm
K_{Ic}	Critical coefficient of grain strain intensity, MPa·m$^{1/2}$
n_{sd}	Grinding wheel rotational speed while dressing, rpm
P	Grinding power, W
Q_d	Diamond dresser mass, kt
Q_C	Grinding fluid, l/min
Q_w	Material removal rate, mm³/s
rms	Root–mean–square roundness deviation from mean circle, μm
Ra	Arithmetic mean deviation of the workpiece roughness profile, μm
Rz	Maximum height of the roughness profile within a sampling length, μm
Sa	Arithmetic mean deviation of the surface, mm
Sdr	Developed interfacial area ratio, %

K. Nadolny (✉)
Department of Production Engineering, Faculty of Mechanical Engineering, Koszalin University of Technology, Racławicka 15-17, 75-620 Koszalin, Poland
e-mail: krzysztof.nadolny@tu.koszalin.pl

Sds	Density of summits of the surface, pks/mm^2
Sm	Mean width of roughness profile elements within a sampling length, μm
St	Total height of the surface, mm
T	Grinding wheel total height in axial direction, mm
Ua	Accelerating voltage, V
v_{fa}	Axial table feed speed while grinding, mm/s
v_{fd}	Axial table feed speed while dressing, mm/s
v_s	Grinding wheel peripheral speed, m/s
v_w	Workpiece peripheral speed, m/s
V_b	Volume of bond in the grinding wheel, %
V_g	Volume of abrasive grains in the grinding wheel, %
V_p	Volume of pores in the grinding wheel, %
V_w	Material removal, mm^3
V_s	Volumetric grinding wheel wear, mm^3
χ	Angle of conic chamfer, °
Δ	Maximum roundness deviation, μm
Δa	Arithmetic mean slope of the roughness profile, °
ΔP	Grinding power gain, W
ΔP_l	Grinding power gain limit, W

1 Introduction

Modern grinding processes provide a high quality of machined surface with constantly improving material removal rates. The quality is obtained by, among other procedures, applying new abrasive materials, developing new kinematic variations, and modifying grinding process parameters or by introducing modifications in the grinding wheel structure. These elements are often interrelated, with, for example, the effective realization of a single working pass of the grinding wheel being connected to the proper modification of the grinding wheel's macrogeometry, i.e., the shaping of the conic chamfer.

Grinding wheels with conic chamfer were developed for the needs of traverse grinding processes, in which the whole machining allowance is removed in a single working pass of the grinding wheel. The most common traverse processes include external cylindrical continuous path-controlled grinding (CPCG), where grinding wheels from superhard abrasive grains are used [1–6]. Methods of traverse grinding with grinding wheels made from Al_2O_3 grains are also being developed [7–11].

In relation to internal cylindrical grinding processes, the subject literature offers only descriptions of processes called peel grinding or internal deep traverse grinding [12], as well as an example of traverse cylindrical grinding with the *Quickpoint* method [13]. This method consists of reducing the area of contact between the grinding wheel and the workpiece to the aforementioned point—hence the name of the

method—by deflecting the grinding wheel axis in relation to the workpiece axis by an angle of $\alpha_k=0.5°$ [14, 15].

Grinding wheels from cubic boron nitride (CBN) with the total height in the axial direction $T<6$ mm, characterized by a conic rough grinding zone, are used in the *peel grinding* and *traverse grinding* processes. Such grinding wheels make it possible to remove the total machining allowance of $a_{e\ tot}=0.15$ mm in a single pass. The grinding power is also decreased and therefore the tendency to shape the conic opening is limited. Moreover, flexibility is improved compared to conventional cylindrical grinding, while the high process reliability and high quality finish workpiece are maintained [12].

The conic chamfer angle χ is crucial to the rough grinding process course, and it is dependent on a number of parameters such as the grinding wheel coasting, volume of the removed machining allowance, grinding wheel height, as well as the requirements concerning surface quality. The latter determines the finish grinding and sparking-out zones' width. As a result of grinding wheel wear, the rough grinding zone is moved into the finish grinding and sparking-out zone, which causes its shortening.

Application of increased grinding speed $v_s=60$-80 m/s and a properly shaped grinding wheel active surface (GWAS) macrogeometry, divided into the conic zone with angle $\chi=5°$ and the cylindrical finish grinding zone (2–4 mm long), enables the achieving of the material removal rate of as much as $Q_w=24$–37.7 mm^3/s. The sparking-out zone, which is then long enough, guarantees the attainment of a machined surface roughness on the level of $Rz<1$ μm [12].

The described grinding wheel geometry makes it possible to increase the material removal rate through increasing the axial table feed speed v_{fa}. Even though this leads to an increased rough grinding zone load, it is possible to obtain a good quality surface thanks to multiple grinding of the workpiece by the cylindrical zone of the finish grinding. As a result, with machining efficiency similar to hard turning, considerably better surface quality is obtained [12].

As up to now mostly expensive grinding wheels from cubic boron nitride, which required specialized grinding machines with considerable stiffness and large grinding speed ($v_s>60$ m/s), have been used in traverse grinding processes, the need to develop new grinding wheel constructions from far cheaper grains that could also be used in traditional grinding machines has arisen.

2 Grinding wheels with Al_2O_3 abrasive grains for internal cylindrical traverse grinding

In the case of the application of cheaper abrasive grains on the basis of Al_2O_3, it was necessary to considerably increase the total grinding wheel height ($T=20$ mm) due to the lower

cutting ability of such abrasives as compared to CBN grains [16–19]. Figure 1 presents a construction scheme (Fig. 1b) and the axial microgeometry profile with conic chamfer (Fig. 1c), designed for traverse internal cylindrical grinding. What is also included are microscopic images of the grinding wheel active surface and single microcrystalline sintered alumina abrasive grains of the SG™ type produced by Norton company (Fig. 1a), which the described grinding wheels were made from.

2.1 Abrasive grains

Sintered microcrystalline alumina is characterized by similar hardness and greater ductility than fused alumina oxide grains, which translates into greater resistance to fragile cracking. Compared to white fused alumina, sintered microcrystalline alumina grains are 10 % harder. Their shape is similar to the typical one but is characterized by greater uniformity of shape and size. The grains are composed of a large number of minor crystallites, connected through a thin crystalline layer (Fig. 2) [20].

As the grains of conventional white fused alumina are characterized by a polycrystalline structure with preferential crystallographic planes, they crack parallel to these planes (the crystallographic layout) under the influence of strain. Such a process results in the loss of considerable grain mass, which is additionally enhanced by defects in the grain that cause microchipping. The dressing process also leads to dulling of the grinding wheel active surface through flattening of the grain corners. The reason for this is the fact that white fused alumina grains are usually single crystallites [16–19, 21].

A sintered microcrystalline alumina grain has a submicrocrystalline structure with particles sized 0.1-5 μm (however, usually <1 μm). For reference, the size of sintered alumina crystallites is similar to the nominal grain size or slightly smaller. Such a structure results in a greater value of the critical coefficient of grain strain intensity K_{Ic}. Proper selection of grinding and dressing parameters makes it possible for the phenomenon of abrasive grain self-sharpening to occur, which is caused by microparticles breaking out from it, which, in turn, lead to the creation of sharp corners and cutting edges. As a result, it is possible to limit the grinding wheel wear through the creation of a greater number of active apexes on its active surface [16–19, 21].

2.2 Glass–crystalline bond

The described grinding wheels were made using glass-crystalline bond from the CMAS system (CaO-MgO-Al_2O_3-SiO_2) [22–24]. It is characterized by good wetting, while the presence of the basic crystalline phase of the pyroxene type improves its resistance to abrasive wear and microhardness of the material as compared to glass bond [25]. Figure 3 presents the phase diagram of the applied bond.

The analysis was made using the X-ray diffractometer Siemens D5000, which utilizes CuK radiation (counting time 5 s, sample rotation 1 rpm, measurement range 10–60 s). The bond diffractometer revealed the presence of two crystalline phases from the pyroxene group, augite and diopside, in the sample.

Table 1 presents the most important structural and physical-chemical properties of the applied glass–crystalline bond as compared to the glass bond (amorphous) and microcrystalline sintered alumina grains.

3 Wear phenomena of the GWAS

The most important GWAS components wear phenomena include abrasive and facture wear [16, 27–29]. These

Fig. 1 Grinding wheel with conic chamfer for internal cylindrical traverse grinding: **a** SEM images of single abrasive grains and grinding wheel active surface, **b** construction scheme, and **c** microgeometrical axial profile of the grinding wheel active surface with an exposed conical chamfer angle χ
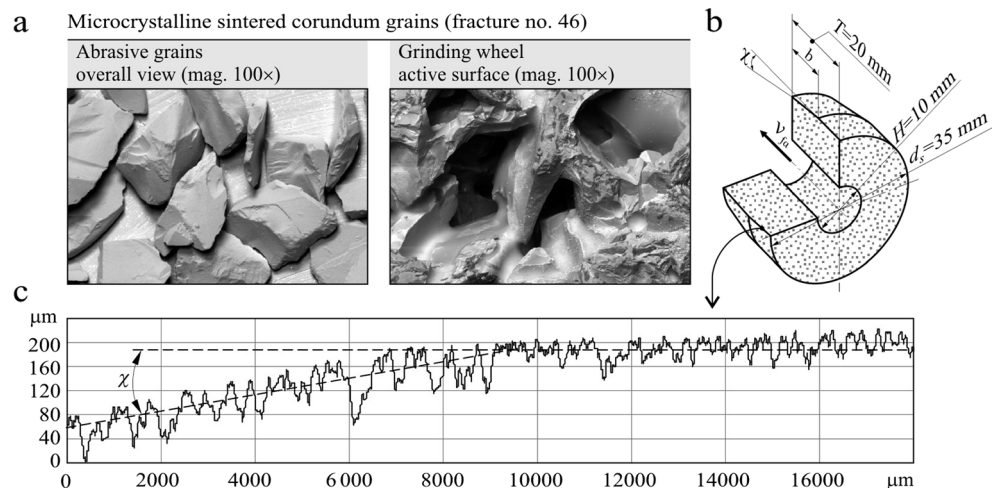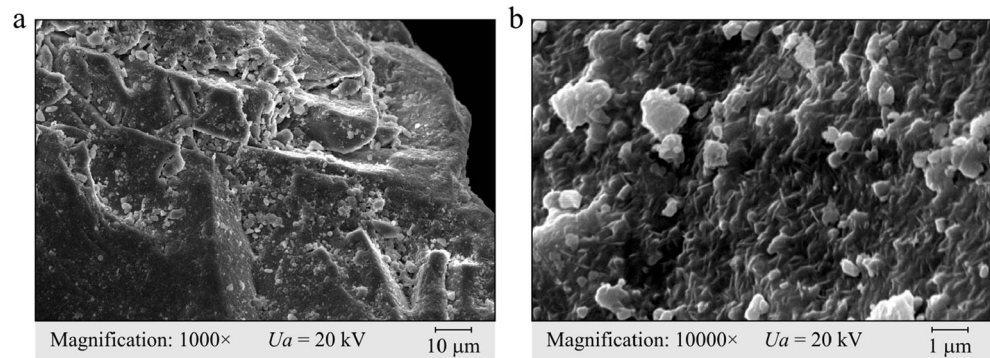
Fig. 2 Microscopic view of the SG™ grains microstructure: **a** magnification ×1000 and **b** magnification ×10,000

Magnification: 1000× $Ua = 20$ kV 10 μm

Magnification: 10000× $Ua = 20$ kV 1 μm

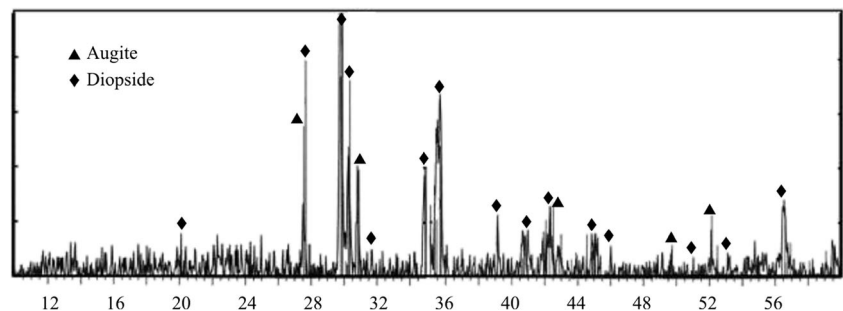processes take place in both the abrasive grains and the bond and therefore the following can be discerned:

– Abrasive wear of the active abrasive grains vertexes,
– Abrasive wear of the bond in the areas of contact with the machined material,
– Fracture wear of the abrasive grains due to mechanical and thermal shock loads,
– Fracture of bond bridges,
– Fracture at the interface between abrasive grain and bond bridge, and
– Smearing of the grain vertexes and intergranular free spaces with the machined material.

Figure 4 presents examples of microscopic views illustrating the basic processes of grinding wheel component wear.

Dulling of the grain vertexes is caused by the abrasive wear and occurs as a result of a number of phenomena occurring on the microscale such as the following [16]:

– Wear due to frictional interaction between workpiece and abrasive grain,
– Plastic flow of the abrasive grain at high temperature and pressure,
– Crumbling of the abrasive grain due to thermal diffusion and microscale mechanical impact, and

– Chemical reaction between abrasive and workpiece material at elevated temperatures and in the presence of grinding fluids.
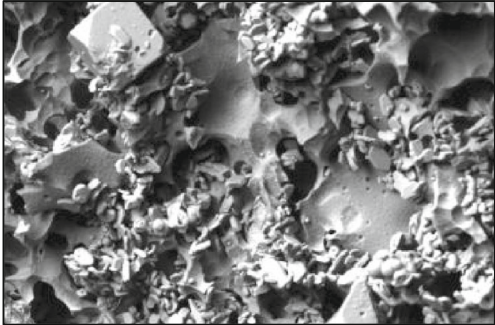
The most important phenomena causing fractures in the form of cracking or chipping of the abrasive grain particles, as well as chipping of the bond particles and fracturing of its bridges, include the following:

– Effective wear caused by the mechanical shock load,
– Fatigue wear caused by recurrent influence of the mechanical shock load, and
– Thermal-fatigue wear in which the fatigue wear is additionally supported by the periodically changeable or intermittent thermal shock load.

4 Experimental tests

When grinding wheels made from conventional abrasive grains (on the basis of Al_2O_3 or SiC) are used in industrial conditions in automated cylindrical grinding (e.g., in the bearing ring industry), the dressing procedure is usually performed after each working pass. Such a strategy is used in order to maintain full repeatability of the machining effects. As a result, most of the grinding wheel volume is lost not because

Fig. 3 X-ray powdered crystal pattern of the glass–crystalline bond, thermally treated at 1000 °C for 1 h, at which point the grinding wheels are produced with this bond—the intensity of the deflected X-ray beam for an angle of beam reflection within the range from 10 to 60° [26]

▲ Augite
◆ Diopside

12 16 20 24 28 32 36 40 44 48 52 56

Table 1 Properties of glass–crystalline vitrified bond

Type of material	Structure	Type and participation of crystalline phase	Average grain size, μm	K_{IC}, MPa·m$^{1/2}$	SEM microscopic view of the structure (partially etched in 10 % solution of HF)
Glass–crystalline	Polymicrocrystalline— amorphous	Augit and diopside 29.02 %	>5	1.15	

Magnification 1000× Ua=20 kV 10 μm

of the wear phenomena but because of the cutting ability being renewed (conditioning, shaping, and sharpening).

Application of grinding wheels with conic chamfer requires far more from the dressing procedures because of the necessity for precise shaping of the grinding wheel macrogeometry. For this reason, it is crucial to look for possibilities to prolong the life of those grinding wheels that

usually work with two or three times greater machining allowance resulting from the traverse grinding process.

The purpose of the experimental tests was to determine the most advantageous volume of glass–crystalline bond from the perspective of extending the grinding wheel life in the process of traverse internal cylindrical grinding of steel 100Cr6. The experiment's results were used to determine the dominant
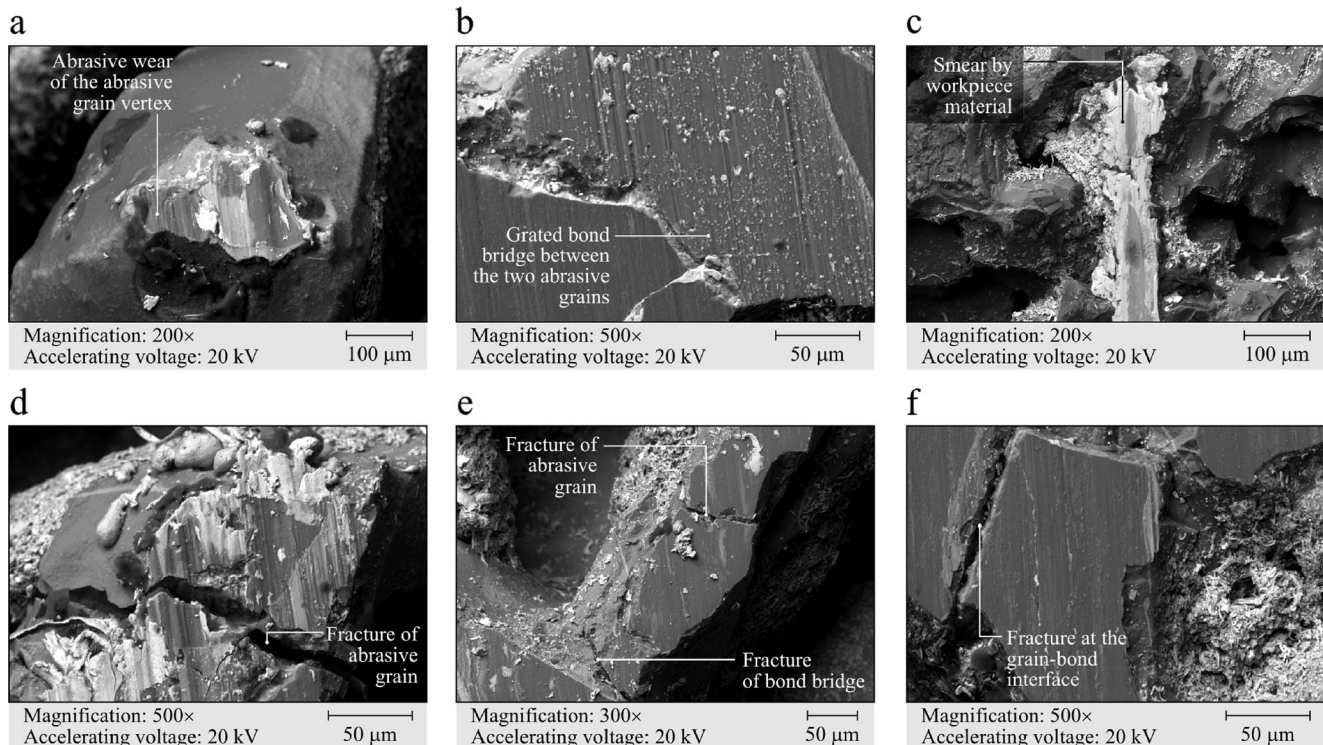
a Abrasive wear of the abrasive grain vertex

Magnification: 200×
Accelerating voltage: 20 kV   100 μm

b Grated bond bridge between the two abrasive grains

Magnification: 500×
Accelerating voltage: 20 kV   50 μm

c Smear by workpiece material

Magnification: 200×
Accelerating voltage: 20 kV   100 μm

d Fracture of abrasive grain

Magnification: 500×
Accelerating voltage: 20 kV   50 μm

e Fracture of abrasive grain / Fracture of bond bridge

Magnification: 300×
Accelerating voltage: 20 kV   50 μm

f Fracture at the grain-bond interface

Magnification: 500×
Accelerating voltage: 20 kV   50 μm

Fig. 4 Microscopic SEM views of the grinding wheel active surface presenting the effects of processes of grinding wheel wear: **a** abrasive wear of vertexes of the active abrasive grains, **b** abrasive wear of bond, **c** smear of abrasive vertexes and intergranular free spaces by workpiece material, **d** fracture of abrasive grains, **e** fracture of bond bridges, and **f** fracture at the boundary between the abrasive grain and bond bridge

Table 2 General characteristics of grinding conditions

Process	Traverse peripheral internal cylindrical grinding
Grinding machine	Universal grinding machine RUP 28P by Mechanical Works Tarnow SA, Poland, equipped with spindle type EV-70/70-2WB produced by Fisher, Switzerland (max. rpm 60 000 1/min, power of machine cutting 5.2 kW)
Dressing parameters	Dresser—single-grain diamond dresser Q_d=1.25 kt, n_{sd}=12 000 rpm, v_{fd}=10 m/s, a_d=0.0125 mm
Grinding parameters	v_s=60 m/s, v_w=0.75 m/s, v_{fa}=2.0 mm/s, a_e=0.20 mm, Q_C=3.0 l/min
Coolant	5 % Water solution of Castrol Syntilo RHS oil given by flood method
Workpiece	Internal cylindrical surface of bearing rings, made of 100Cr6 steel (63±2 HRC), internal diameter d_w=40 mm, width b_w=18 mm

phenomena of the wear of the active surface of grinding wheels with conic chamfer and the influence of the bond volume changes on their intensity.

4.1 Methodology of experimental tests

The experimental tests were carried out on a station equipped with a universal grinding machine RUP-28P. The applied values of the key machining parameters (a_e=0.20 mm and v_{fa}=2.0 mm/s) correspond to grinding with material removal rate Q_w≈24 mm³/s. What was registered during the tests were a grinding power ΔP, root-mean–square roundness deviation from mean circle (Δ, rms), and grinding wheel outer diameter changes d_s, which were indicative of the volume wear V_s. The grinding wheel outer diameter was measured on the cylindrical part, while the perimeter profiles in the roundness error measurements were registered on the conic and the cylindrical areas of the grinding wheels. After the trials were finished, workpiece surface roughness parameters were determined,

microtopography measurements were made, and the SEM observations of the examined grinding wheel active surfaces were performed.

Exceeding the limit value of grinding power gain ΔP_l=1000 W, which was determined on the basis of previous research on traverse internal cylindrical grinding with such grinding wheels [30, 31], was adopted as the criterion of cutting ability loss and the end life of the examined grinding wheels. It was agreed that over that value, the risk of defects appearing on the workpiece surface in the form of grinding burns increased dramatically. Table 2 includes a presentation of the conditions of the performed experimental tests.

4.2 Grinding wheels

Three variations (C1, C2, and C3) of the type 1 grinding wheel sized $35 \times 20 \times 10$ mm were used in the tests, which were made from microcrystalline sintered alumina grains SG™ number 46 and glass–crystalline bond. The three variations differed only in the bond volumes which were V_b=14.5 % (grinding wheel C1), V_b=13.0 % (grinding wheel C2), and V_b=11.5 % (grinding wheel C3), which corresponded to three classes of grinding wheel hardness M, L, and K, respectively. Conic chamfer with the angle χ=0.72° and width b=16 mm, selected according to the machining allowance (a_e=0.20 mm), was shaped on the grinding wheel active surfaces.

In order to make quick shaping of the conic chamfer with specific geometrical parameters on the grinding wheel active surface possible, it was necessary to develop a special automated dressing device [32]. The most important element of the device, as presented in Fig. 5, is the sliding table on ball slideways to which the blade mounting of the single-grain diamond dresser and the micrometric screw, which was used for precise setting-up of the conic chamfer angle, were fixed.

The theoretically and experimentally determined precision of conic chamfer shaping in the range χ=0-1.5° is approximately ±3 % [33]. Table 3 presents the characteristics of the three grinding wheel variations used in the experimental tests.

Fig. 5 Device for precision shaping of the conic chamfer on the grinding wheel active surface: **a** functional elements and **b** view of the test-ready device [32]
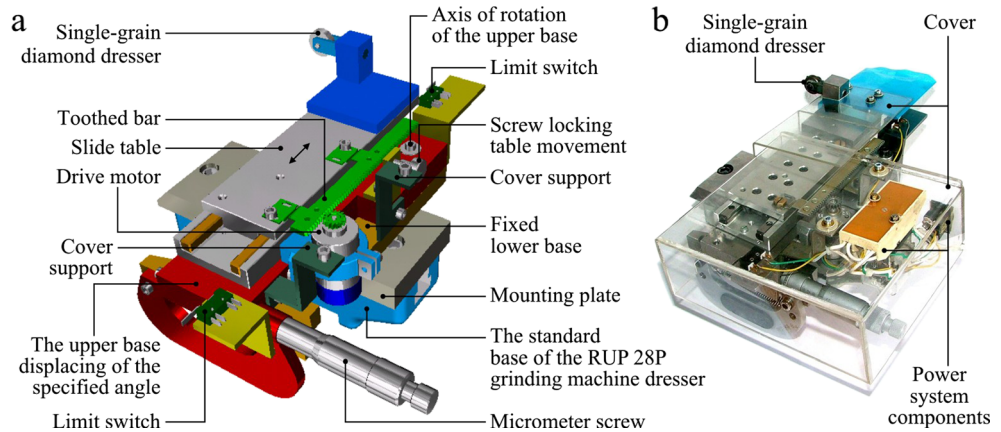
Table 3 Characteristics of grinding wheels used in the experiments

Short name	Grinding wheel C1	Grinding wheel C2	Grinding wheel C3
Technical designation	1–35×20×10-SG/F46K7VTO	1–35×20×10-SG/F46L7VTO	1–35×20×10-SG/F46M7VTO
Volume of grains (V_g)	48.0 %	48.0 %	48.0 %
Volume of bond (V_b)	14.5 %	13.0 %	11.5 %
Volume of pores (V_p)	37.5 %	39.0 %	40.5 %
Hardness class	M	L	K
Grinding wheel type	1—flat grinding wheel		
Dimensions	External diameter d_s=35 mm, height T=20 mm, inner diameter H=10 mm		
Abrasive grain type	Microcrystalline sintered alumina SG™ by Norton (USA)		
Abrasive grain fracture no.	46		
Structure no.	7		
Bond type	Vitrified (V) glass–crystalline bond type TO		
Conic chamfer parameters	Chamfer angle χ=0.72°, chamfer width b=16 mm		

4.3 The applied measuring systems

The grinding results were analyzed, and the grinding wheel active surface wear phenomena were identified on the basis of the measurements and observations carried out using a variety of modern measurement systems. The machined surface roughness parameters were determined on the basis of the profiles registered by stylus profilometer Hommel-Tester T8000 by Hommelwerke GmbH (Germany). The grinding wheel active surface microtopographical measurements were made using the multi-head measuring system Talysurf CLI 2000 by Taylor-Hobson Ltd. (UK), which performs the measurement using the laser triangulation method. The GWAS microscopic images were registered on the scanning electron microscope JSM-5500LV by JEOL Ltd. (Japan). The correct identification of objects observed on the SEM images was confirmed with an energy-dispersive X-ray spectroscopy (EDS) module INCAPentaFET-x3 from Oxford Instruments (UK). Values of the grinding wheel roundness errors were determined with the roundness measuring instrument Rondcom 44 by Carl Zeiss AG (Germany). Moreover, in order to estimate the edge wear, the microgeometry of the axial profile of the grinding wheels with conic chamfer was measured on bench-type multisensor coordinate measuring machine VideoCheck-IP 250, produced by Werth Messtechnik GmbH (Germany).
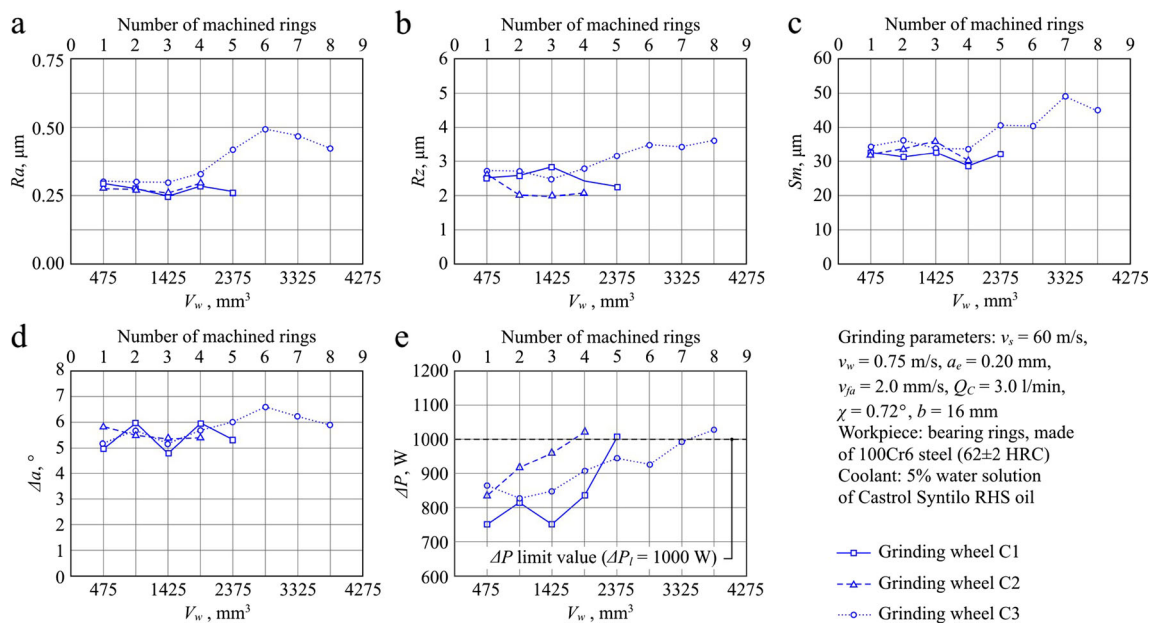

Fig. 6 Changes of values of the selected workpiece surface roughness parameters and grinding power gain ΔP over material removal V_w during internal cylindrical traverse grinding using tested grinding wheels: **a** arithmetic mean deviation of the workpiece profile Ra; **b** maximum height of the profile within a sampling length Rz; **c** mean width of profile elements, within a sampling length Sm; **d** arithmetic mean slope of the profile Δa; and **e** grinding power gain ΔP

Grinding parameters: v_s = 60 m/s, v_w = 0.75 m/s, a_e = 0.20 mm, v_{fa} = 2.0 mm/s, Q_C = 3.0 l/min, χ = 0.72 °, b = 16 mm
Workpiece: bearing rings, made of 100Cr6 steel (62±2 HRC) | Coolant: 5% water solution of Castrol Syntilo RHS oil
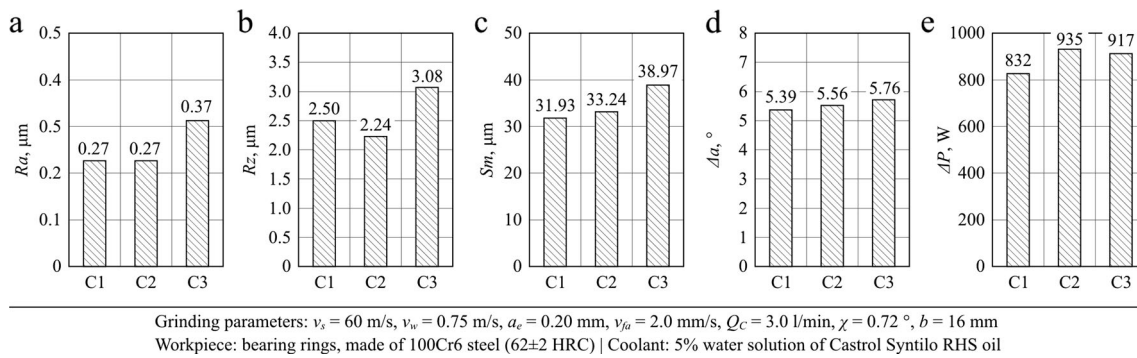
Fig. 7 Averaged values of the selected workpiece surface roughness parameters and grinding power designated for the whole durability period of the tested grinding wheels: **a** arithmetic mean deviation of the workpiece profile Ra; **b** maximum height of the profile within a sampling length Rz; **c** mean width of profile elements, within a sampling length Sm; **d** arithmetic mean slope of the profile Δa; and **e** grinding power gain ΔP

4.4 Test results

Figure 6 presents charts illustrating the changing values of selected post-grinding surface roughness parameters (Ra, Rz, Sm, Δa) and the grinding power gain ΔP in the function of machined material removal V_w.

The test results obtained show that the C3 grinding wheel, characterized by the lowest bond volume V_b=11.5 %, had the longest life. It was used for grinding eight rings until the grinding power limit value ΔP_l=1000 W was exceeded. The remaining grinding wheels, with greater bond volume, were used to process only between 4 and 5 rings (Fig. 6).

The charts illustrating the changing values of the selected parameters describing machined surface roughness, included in Fig. 6a-d, indicate that satisfactory surface roughness was obtained for all grinding wheels. What is also crucial are the minor dispersions in the values of the determined parameters, which indicate the repeatability of the obtained machining effects. The tendency to rise along with the grinding wheel operating time prolongation is visible; however, the tendency is relatively minor. The greatest influence of the changes caused by the grinding wheel component wear on the grinding course can be observed in the chart covering grinding power gain ΔP (Fig. 6e). This parameter reacts with great precision to any increase of friction in the machining process, which is indicative of dulling of the abrasive grain vertexes on the GWAS.

Figure 7 presents a comparison of the mean values of the assessed grinding parameters from the whole life of the examined grinding wheels. The charts presented in Fig. 7 show that as the grinding wheel operating time increases, the mean values of the machined surface roughness parameters grow (Fig. 7a–d). The ranges of these changes were, respectively, ≈37 % for parameters Ra and Rz, ≈37 % for parameter Rz, ≈22 % for parameter Sm, and ≈7 % for parameter Δa. The mean value of grinding power gain was insignificant and (within the range of 832-935 W) without any visible tendency (Fig. 7e).

Figure 8 presents a comparison of the total material removal volume V_w (Fig. 8a), volumetric grinding wheel wear V_s (Fig. 8b), and the G-ratio $G=V_w/V_s$ (Fig. 8c) obtained with the applied grinding wheels. Analysis of the charts presented in Fig. 8 shows that for all grinding wheels, the G-ratio barely changed and ranged from 118.9 (grinding wheel C1) to 93.6 (grinding wheel C3), while a decreasing tendency in the function of decreasing the volumetric share of the bond is visible.

Figure 9 contains charts presenting changes in values of parameters describing root–mean–square roundness deviation from the mean circle (Δ, rms) measured on the conic and cylindrical areas of the examined grinding wheels with the registered peripheral profiles. The initial values (Fig. 9a), corresponding to V_w=0 mm³ (measured after the dressing procedure), were compared with the values determined on
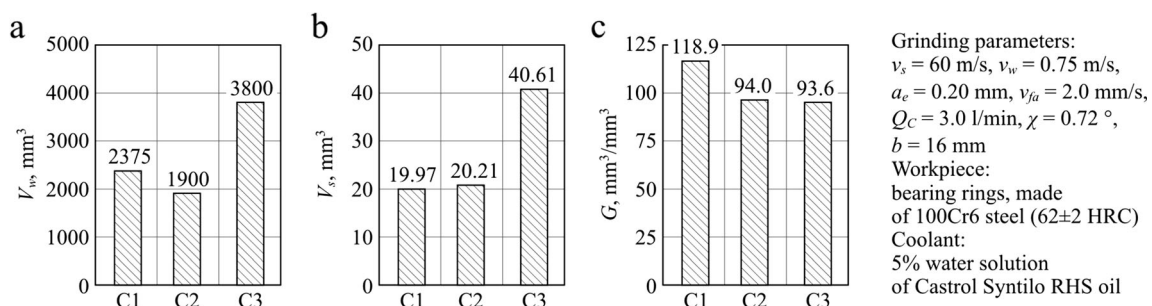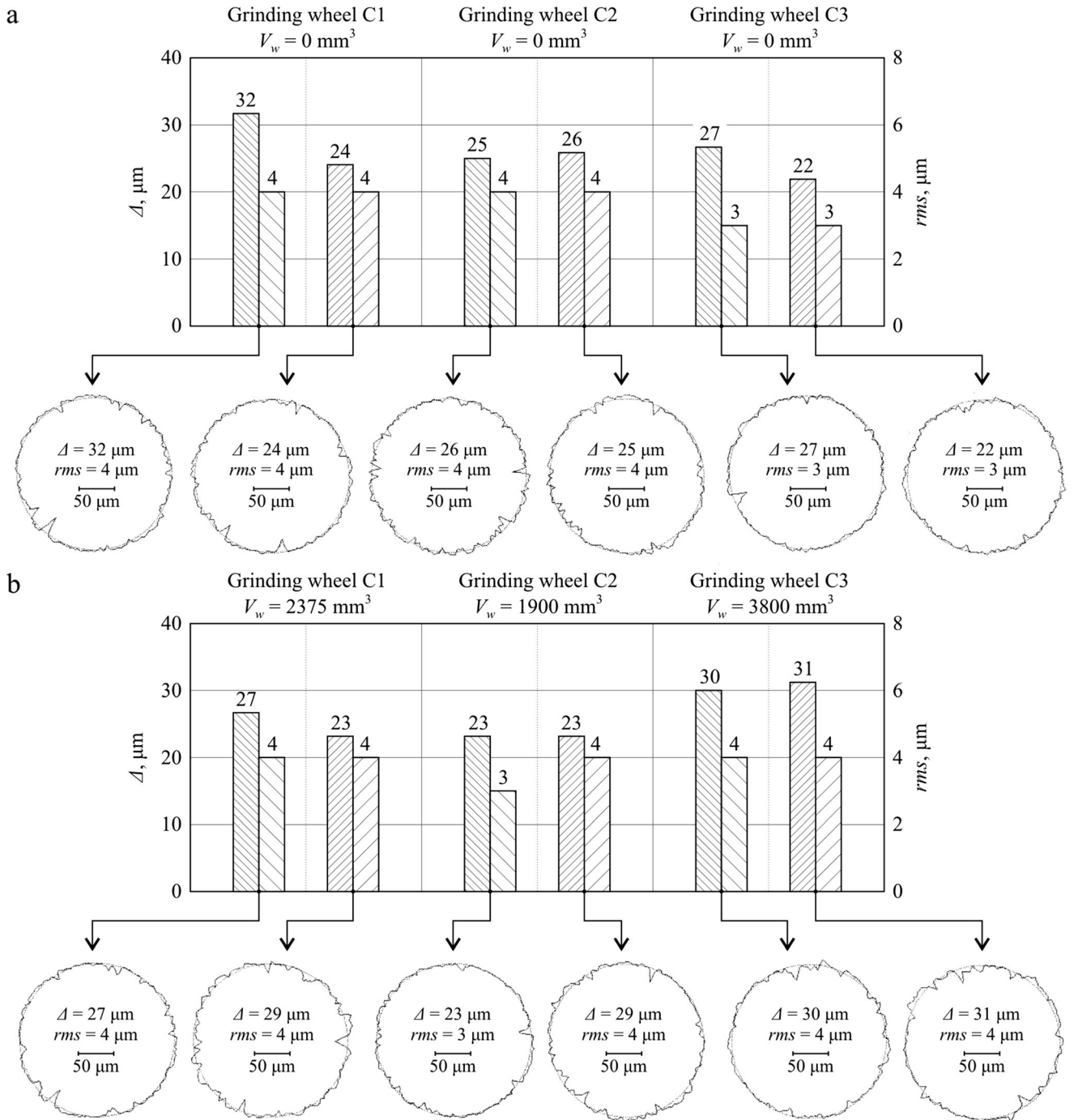

Grinding parameters:
v_s = 60 m/s, v_w = 0.75 m/s,
a_e = 0.20 mm, v_{fa} = 2.0 mm/s,
Q_C = 3.0 l/min, χ = 0.72 °,
b = 16 mm
Workpiece:
bearing rings, made
of 100Cr6 steel (62±2 HRC)
Coolant:
5% water solution
of Castrol Syntilo RHS oil

Fig. 8 Designated values of material removal V_w (**a**), volumetric grinding wheel wear V_s (**b**), and G-ratio (**c**) after the end of the tested grinding wheel life

the basis of grinding wheel measurements after termination of their lives (Fig. 9b).

In the case of C1 and C2 grinding wheels, a slight decrease in the value of parameters describing root–mean–square


Fig. 9 The changing values of the maximum roundness deviation Δ and root–mean–square deviation from the mean circle rms and circumference profile of the tested grinding wheels, measured using roundness measuring instrument Rondcom 44 by Carl Zeiss AG: **a** after dressing and **b** at the end of life

Fig. 10 Axial profiles of the tested grinding wheel active surfaces at the end of life: **a** grinding wheel C1, **b** grinding wheel C2, and **c** grinding wheel C3 (measured using bench-type multisensor coordinate measuring machine VideoCheck-IP 250 by Werth Messtechnik GmbH)
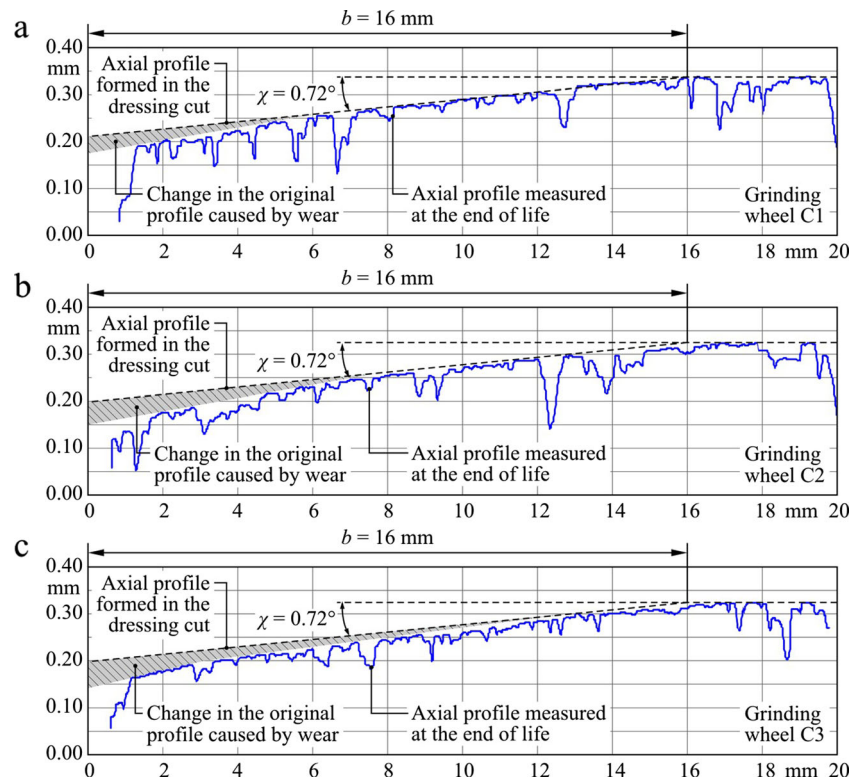
roundness deviation from the mean circle after grinding is visible (Fig. 9b), as compared to the values determined after the dressing procedure (Fig. 9a). The case is different when it comes to the C3 grinding wheel which remained operational the longest. The measured Δ values after work are considerably greater than after dressing for the C3 grinding wheel, especially in the most loaded rough grinding conic zone (Δ=22 μm after dressing and Δ=31 μm after termination of life).

A comparison of the registered axial profiles of the examined tools after work (Fig. 10) shows that as the bond volume decreases, the grinding wheel edge wear increases. The greatest change in the shape of the axial outline, shaped in the dressing procedure, relates mostly to the conic area, which

is most loaded because of the rough grinding procedure. The outline of the C3 grinding wheel (Fig. 10c) becomes considerably more visible the more smoothed out the active abrasive grain vertexes are at the beginning of the conic zone, as compared to grinding wheels C1 and C2 (Fig. 10a–b).

The comparison of macrotopographies of the active surfaces of the examined grinding wheels before and after the machining (Fig. 11) shows that in the case of grinding wheels C1 and C2 after work wear smears/loads the intergranular free spaces with machined material chips (Fig. 11a–b). The surface of these grinding wheels is dark, which means that ground products remain in the intergranular free spaces. Figure 11c, which presents the C3 grinding wheel surface, does not have
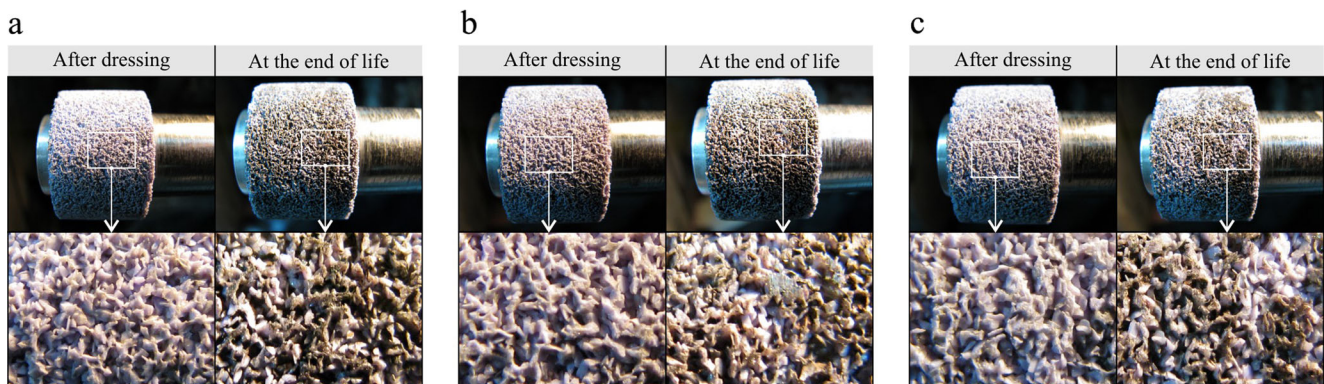

Fig. 11 Macroscopic images of the active surface of the tested grinding wheels after dressing and at the end of life: **a** grinding wheel C1, **b** grinding wheel C2, and **c** grinding wheel C3

visible smears/loads, while lighter areas are visible, which result from new cutting vertexes being revealed as a result of microchipping of the active abrasive grains and glass-crystalline bond bridges.

Figure 12 presents the registered GWAS microtopographies after grinding, alongside the values of the selected roughness parameters, as well as analyses of islands with the threshold value of 0.2 mm from the highest topographical point.

The comparison of the Sa and St parameter values shows that all the grinding wheels were characterized by similar heights of active surface unevenness after work, while the greatest Sa value was determined for the C3 grinding wheel (Fig. 12c). Greater differences were noted for the values of developed interfacial area ratio Sdr and density of summits of the grinding wheel active surface Sds. What is clearly visible in the case of both parameters is the growing
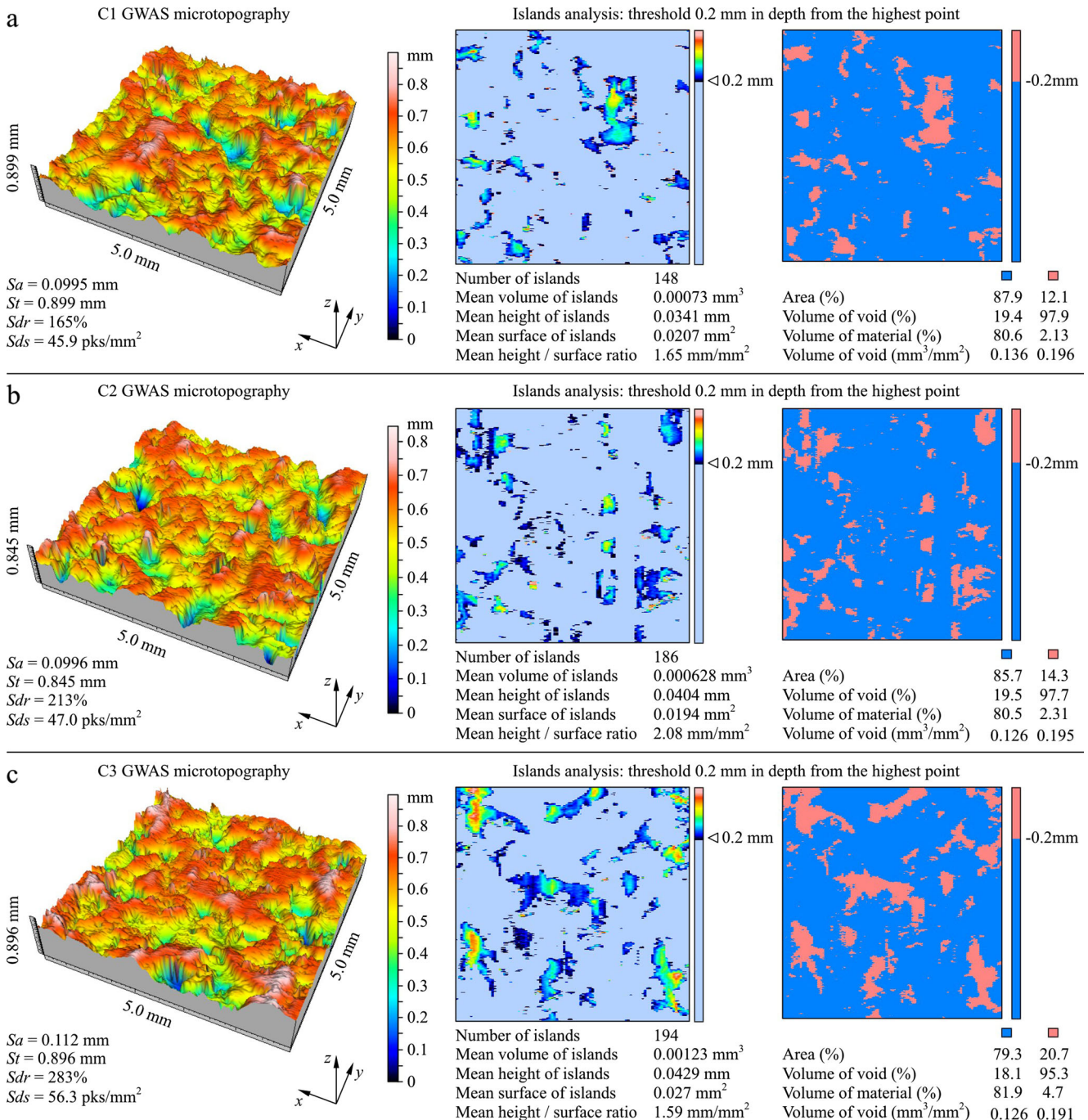

Fig. 12 Collection of selected analyses of microtopographies of the tested grinding wheels at the end of life: **a** grinding wheel C1, **b** grinding wheel C2, and **c** grinding wheel C3 (measured using multi-head measuring system Talysurf CLI 2000 by Taylor-Hobson Ltd.)

tendency for a progressive decrease of the bond volume in the grinding wheel.

Moreover, the island analysis was carried out in order to determine a group of parameters describing the geometric features of the active abrasive grain vertexes and the intergranular spaces. It shows that as the bond volume decreases, the active surface of the examined grinding wheels, after work, is characterized by a greater number and volume of the abrasive grain vertexes.

In order to perform the visual evaluation of the condition of the examined grinding wheels' active surface, SEM observations were carried out, whose selected results are compared in Fig. 13.

The SEM images show the majority of abrasive wear of the active abrasive grain vertexes. Moreover, in the areas of the GWAS contact with the machined surface, microsmearings with chips of the machined material and grinding wheel wear products, such as chipped bond and grain fragments, were created. The chips located in the grinding zone were embrocated into the microfractures located on the smoothed-out grain surface. However, no extensive intergranular free space smearings were observed. What was noticed on the surface of all examined grinding wheels were chips of the machined material characterized by a continuous shape, resulting from the characteristics of the machined steel 100Cr6, as well as significant size diversification. Also visible are chips the length of 150 μm shaped during rough grinding, as well as microchips the size of a few micrometers, created during the last stage of the machining process, when sparking out of the surface takes place. There were also spherical chips on the surfaces of the C1 and C2 grinding wheels (Fig. 13c, d, g), and melted machined material congealed on the smoothed-out abrasive grain vertex was observed (Fig. 13h).

4.5 Discussion of the test results

The test result comparison presented in Section 4.4 allowed for a multicriterion evaluation of the grinding wheel surface element wear phenomena in the process of traverse internal cylindrical grinding in steel 100Cr6 with increased material removal rate. Among the three grinding wheels selected for the tests, the longest life was registered in the C3 grinding wheel (Fig. 6), characterized by the lowest volume of glass–crystalline bond V_b=11.5 %. It can be therefore assumed that minimizing the bond volume in the grinding wheel contributes to easier chipping of the dulled abrasive grain microvertexes that result from reductions in the abrasive grain binding strength. As a result, the C3 grinding wheel maintained its cutting ability for approximately twice as long than in the case of grinding wheels with greater bond volume (C1 and C2). The expected workpiece top layer properties were maintained, along with its geometry and low roughness (Fig. 7a–d),

without a noticeable influence on the grinding power (Fig. 7e) and with only a slight decrease of the obtained G-ratio (Fig. 8c).

In the case of the greater bond volume (grinding wheels C1 and C2), the grains were held in place by the bond bridges for a longer period of time, which contributed to the smoothing out of the active abrasive grain vertexes and simultaneous decrease in the intergranular space depth. As a result, limitation of the root–mean–square roundness deviation from the mean circle was observed, both in the conic and the cylindrical zones of these grinding wheels. The C3 grinding wheel worked for the longest duration, and it also registered the greatest volume wear (V_s=40.61 mm^3, Fig. 8b), as a result of which the circumferential outline geometry was most influenced, as compared to the other examined grinding wheels, by the wear phenomena. The shaped GWAS microgeometry was characterized by a greater root–mean–square roundness deviation from the mean circle values and visibly greater free intergranular spaces (Fig. 9b) than after dressing (Fig. 9a). This is indicative of a progressive bond bridge microchipping process caused by the wear of the active abrasive grain vertexes. This also contributed to the greatest change of the C3 grinding wheel axial outline shape in relation to the initial conic chamfer outline shaped in the dressing procedure (Fig. 10c).

The microscopic view of the C3 grinding wheel after grinding was characterized by the occurrence of brighter areas, which resulted from new cutting vertexes being revealed (Fig. 11c), which were visible on the surfaces of C1 and C2 grinding wheels (Fig. 11a–b). Moreover, the parameters determined, on basis of the grinding wheel surface microtopographies, showed that the C3 grinding wheel was characterized by the greatest number of vertexes (Sds=56.3 pks/mm^2), the greatest developed interfacial area ratio (Sdr=283 %), the greatest number (194) and volume of islands (0.00123 mm^3), as well as the greatest surface share of the islands (20.7 %) from all of the examined tools (Fig. 12). This means that for the examined grinding process, with the applied parameters, the active abrasive grain vertexes and bond bridge load made it possible to partially renew the C3 grinding wheel cutting ability during a relatively long work period.

The long working life of abrasive tools with microcrystalline sintered corundum grains is mostly dependent on the conditions in which the grains work and on the dominant wear processes, including the complex system of phenomena combining the effects of chipping, plastic deformations, and chemical reactions [34, 35]. The microfractures existing in the abradant develop into fracture systems when the strains grow to the critical value, which further leads to chipping of grain microfragments [36]. The grains of microcrystalline aluminum oxide can also be worn out as a result of plastic deformations, which result from slippage and twinning of single
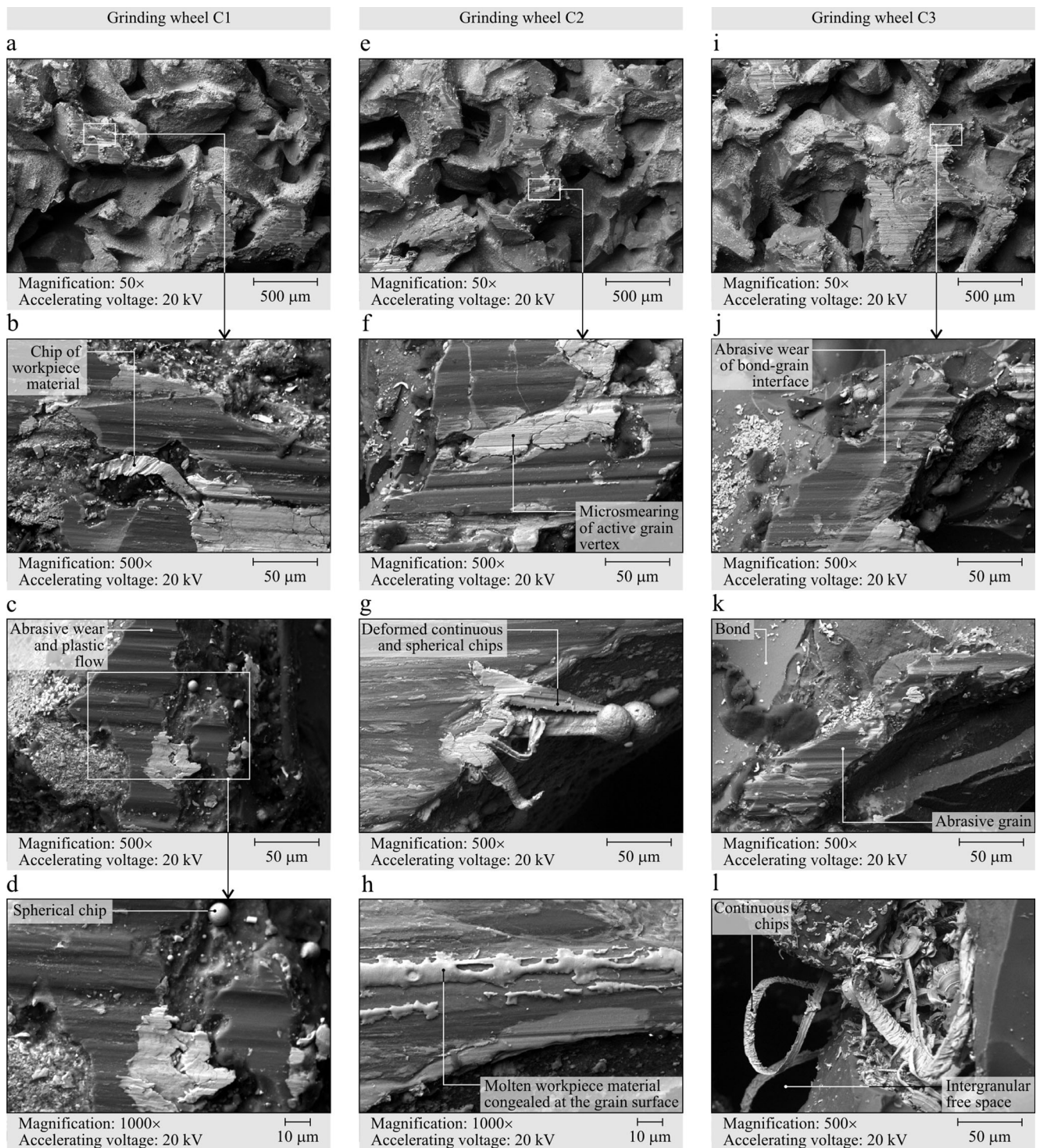
Fig. 13 SEM microscopic images of the GWAS at the end of life of the C3 grinding wheel: **a–d** grinding wheel C1, **e–h** grinding wheel C2, and **i–l** grinding wheel C3 (images taken using scanning electron microscope JSM-5500LV by JEOL Ltd.)

allotriomorphic grains [37]. It was also proved that with the limited number of slip systems, the intensity of grain wear is highly dependent on the crystals' orientation [38]. The process of plastic deformations of the polycrystalline alumina is closely related to the size of crystals and level of strain [39, 40]. As the crystals and their load get smaller and smaller, the grain

deformation process changes from the dominant slippage into diffuse creep and slippage along the crystal edges. However, only recently have the processes of microcrystalline sintered corundum grain wear become recognized. Existing descriptions have mainly focused upon grain crystal microchipping and their self-sharpening through the revealing of numerous

sharpened corners. Most works omitted, however, the relationship between the chipping, plastic deformations, and diffusion that take place on the active abrasive grain vertexes.

Works [34, 35] were the first to present the processes of grinding and Al_2O_3 grain wear in the microcrystalline structure in a detailed and comprehensive way. They showed that the excellent cutting properties of these grains are closely connected with the tribological properties of the smoothed-out cutting vertex surfaces in the area of contact with the machined material. Under the influence of strain and temperature, the vertexes of the microcrystalline sintered corundum abrasive grains are subject to plastic deformation, thus creating flat surfaces of contact with the machined material. The contact of the abrasive grain vertex with the machined material causes dispersion of a large amount of energy as well as a local temperature rise, which causes melting of its surface layer. The alloy is composed of a lowest melting temperature phase, which in the case of 100Cr6 steel results in the creation of iron oxide FeO, in the liquid phase, with high cohesiveness. This limits both the wear and the friction coefficient in the contact area dramatically.

The catastrophic chipping of the largest grain fragments is slowed down on the microcrystalline borders, thanks to which the fractures remain close to the surface and do not propagate into the grain as in the case of the polycrystalline Al_2O_3 grains. The excellent cutting ability of the microcrystalline grains can also be explained by the stable conditions of slippage on flat grain surfaces, created behind the cutting edges.

This research presents results which confirm such a model of microcrystalline sintered corundum grains and indicate that the dominant phenomena of wear of the active microcrystalline abrasive grain vertexes end with the creation of flat

surfaces as a result of abrasive wear and plastic flow. This phenomenon was common on the active surfaces of all the examined grinding wheels and did not have a negative influence on the obtained material removal rate or the quality of the machined surface. The presence of spherical chips on the surfaces of C1 and C2 grinding wheels (Fig. 13c, d, g), as well as signs of the melted machined material (Fig. 13h), is indicative of very high temperatures in the microareas of contact between the abrasive grains and the workpiece. It needs to be assumed that the chip temperature temporarily reached the ground steel melting temperature (1425-1540 °C [41]), causing formation of spherical chips that were empty inside and whose shape results from the surface strain of the liquidized steel. This confirms the possibility of plasticizing the active SG grain vertexes, whose crystals are physically stable up to the temperature of 1500-1700 °C [42]. It was also observed that the phenomenon of shedding the oxide layer and the plastically deformed grain layer occurs periodically on the smoothed-out surfaces of active cutting vertexes. This process is caused by fracture wear (mostly fatigue and thermal-fatigue) as a result of which the sharp crystal edges, located below the plastically deformed surface layer, are revealed (Fig. 14).

Bridges of the glass–crystalline bond, which were characterized by an approximately 30 % volume of the crystalline phase (composed of diopside and augite crystals), were worn out mostly as a result of the abrasive wear caused by their interactions with the machined surface. Analysis of the experiment's results show that for grinding wheels C1 and C2, the fracture wear share was low and was due mainly to the bond's resistance to fracture spreading, caused by the inclusion of the crystalline phase that has a significant influence on the bond's

Fig. 14 Grain wear models in grinding wheels with microcrystalline alumina abrasives (based on drawings Rappold Winterthur Group and the author's own material)
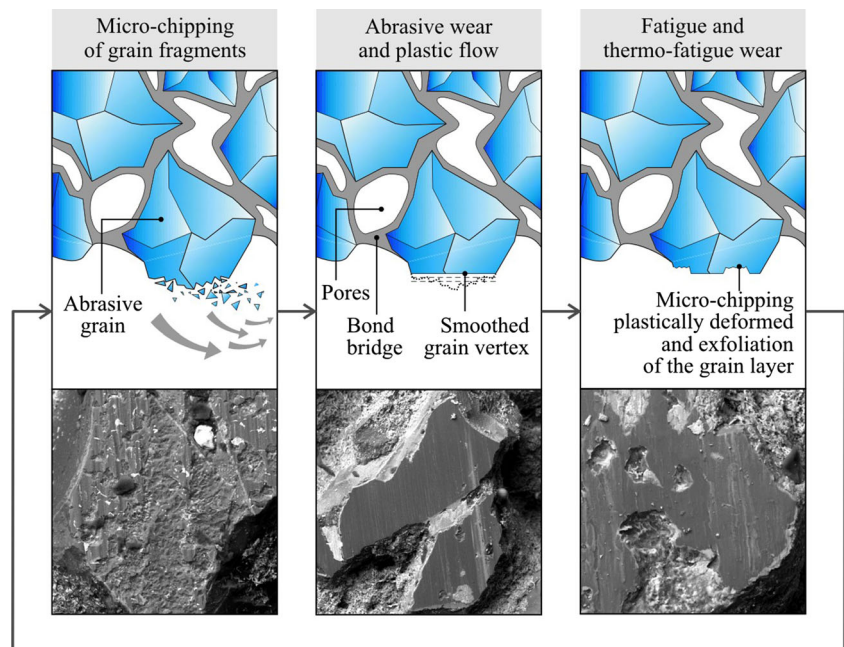
mechanical properties (K_{IC}=1.15 MPa·m$^{1/2}$). By limiting the bond volume to 11.5 % of the grinding wheel (grinding wheel C3), a similar effect to the intensity of wear phenomena occurrence, in the abrasive grains and in the bond, was obtained, which facilitated the periodical renewal of the grinding wheel active surface cutting ability, which took place in microareas of the abrasive grains and the bond.

5 Conclusions

Proper selection of the proportions of particular grinding wheel components (abrasive grains, bond, and intergranular free spaces) affects the tool structure and hardness. The presented tests were aimed at determining the extent to which changing the bond volume within the range of V_b=11.5–14.5 % (which corresponds to a change of the grinding wheel hardness from class K to M) influenced the wear phenomenon of the microcrystalline sintered corundum abrasive grains and ceramic bond bridges with glass-crystalline structure.

The tests were carried out in the process of traverse internal cylindrical grinding in steel 100Cr6, characterized by a relatively high material removal rate (Q_w≈24 mm^3/s) and difficult realization conditions, resulting from the long area of contact between the grinding wheel and the machined material.

Comprehensive analysis of the test results obtained allowed for formation of the following conclusions:

- The longest grinding wheel life was reached in the process of grinding with the grinding wheel possessing the lowest bind volume (C3), which resulted from the change in the share of the dominant wear phenomena taking place on the GWAS;
- In the case of grinding wheels C1 (V_b=13.0 %) and C2 (V_b=14.5 %), the dominant phenomena were the abrasive wear and plastic flow of the active abrasive grain vertexes, accompanied by the creation of microsmearings of the grinding products in the area of contact between the grinding wheel and the machined material. The excessive force of grain binding by the bond bridges did not make it possible to renew the grinding wheel cutting ability and thus enable abrasive grain vertexes self-sharpening. As a result, the significant share of friction in the material removal process, alongside the simultaneous hindering of the provision of the coolant, caused increased temperatures in the microareas of the active abrasive grain vertexes contact, as proven by the presence of spherical chips on the GWAS;
- Analysis of the wear marks on the C3 grinding wheel active surface (V_b=11.5 %), combined with the other test results, made it possible to conclude that in this case, the process for cyclical revealing of new, sharp cutting edges

on the surface of microcrystalline sintered corundum grains took place. The weakening of the grain binding force, resulting from limitation of the bond volume in the grinding wheel, allowed for a twofold prolongation of the grinding wheel life. This was caused by limiting the share of the abrasive wear and plastic flow phenomena, as well as a greater occurrence of the fracture wear, mostly fatigue and thermal-fatigue. In turn, this led to periodic shedding of the oxide layer and the plastically deformed grain layer, as well as to the revealing of the crystals' sharp edges, located below the plastically deformed surface layer.

References

1. Frick W (2004) Glatter rundschliff. Maschinenmarkt 110(13):S34–S37
2. Hegener G (2000) In einem Zug geschliffen. Wellenförmige Werkstücke flexibel und mit hoher Leistung schleiftechnisch bearbeiten. Maschinenmarkt 106(16):38–43
3. Lütjens P (2001) Hard turning or grinding—which is the more economical alternative? IDR 61(1):22–26
4. Lütjens P, Mushardt H (2004) Grinding out hardened parts. Am Mechanist 148(3):52–59
5. Webster J, Tricard M (2004) Innovations in abrasive products for precision grinding. CIRP Ann 53(2):597–617
6. Xingas A (1999) Next generation grinding. Am Mechanist 143(9): 58–64
7. Nakajima T, Okamura K, Uno Y (1984) Traverse grinding techniques for improving both productivity and surface finish. International Grinding Conference, Fontana, Wisconsin, SME, Mr 84–534, Aug. 27–29
8. Herman D, Plichta J, Nadolny K (2006) New ceramic abrasive tools for rough and finishing grinding in one pass. Mater Sci Forum 526: 163–168
9. Nadolny K, Herman D, Plichta J (2006) New generation of zonal diversified structure grinding wheels with microcrystalline aluminium oxide grains (SG) for single-pass internal grinding process. Adv Manuf Sci Technol 30(1):5–12

10. Nadolny K (2012) The effect of integrating the structural modifications of the grinding wheel upon the internal cylindrical grinding process. Arch Civ Mech Eng 12(1):60–67

11. Nadolny K (2013) Microdiscontinuities of the grinding wheel and their effects on its durability during internal cylindrical grinding. Mach Sci Technol 17(1):74–92

12. Weinert K, Finke M, Kötter D (2003) Wirtschaftliche Alternative zum Hartdrehen. Innenrund-Schälschleifen steigert Flexibilität beim Schleifen von Futterteilen. Maschinenmarkt 109(48):44–47

13. Junker E (1985) Verfahren und Vorrichtung zum Hochgeschwindigkeits-Profilschleifen von rotations-symmetrischen Werkstücken. European Patent No. 0176654

14. Klocke F, Bücker C (1996) Quickpoint-Schleifen: Baustein einer flexiblen Produktion. Komplettbearbeiten in nur einer Aufspannung. Ind Anz 118(43–44):48–49

15. Tönshoff HK, Karpuschewski B, Mandrysch T, Inasaki I (1998) Grinding process achievements and consequences on machine tools challenges and opportunities. CIRP Ann 47(2):651–668

16. Jackson MJ, Davim JP (2010) Machining with abrasives. Springer, New York

17. Klocke F (2009) Manufacturing processes 2: grinding, honing, lapping. Springler-Verlag, Berlin

18. Marinescu ID, Hitchiner M, Uhlmann E, Rowe WB, Inasaki I (2007) Handbook of machining with grinding wheels. CRC Press, Boca Raton

19. Rowe WB (2009) Principles of modern grinding technology. William Andrew, Burlington

20. Helletsberger H, Noichl J (1993) Einsatzbereiche von Schleifstoffen. Grenzwerte und Wirtschaftlichkeit von Korund, Sinterkorund und CBN. Tech Rundsch 85(13):24–28

21. Matsuo T (1993) Recent researches on high efficiency and heavy duty grinding. Int J Jpn S Precis Eng 27:303–306

22. Herman D (1998) Glass and glass-ceramic binder obtained from waste material for binding alundum abrasive grains into grinding wheels. Ceram Int 24(7):515–520

23. Herman D, Markul J (2004) Influence of microstructures of binder and abrasive grain on selected operational properties of ceramic grinding wheels made of alumina. Int J Mach Tool Manu 44:511–522

24. Herman D, Plichta J, Karpiński T (1997) Effect of glass-crystalline and amorphous binder application to abrasive tools made of microcrystalline alumina grains type SG. Wear 209:213–218

25. Yekta Eftekhari B, Alizadech P, Rezazadeh L (2007) Synthesis of glass-ceramic glazes in the ZnO-Al$_2$O$_3$-SiO$_2$-ZrO$_2$ system. J Eur Ceram Soc 27:2311–2315

26. Okupski T, Herman D, Walkowiak W, Nadolny K (2012) Influence of spinel phase on selected thermal properties of glass-ceramic materials from the ZAS system. Ceram Mater 64(1):71–77 (In Polish)

27. Jackson MJ, Mills B (2004) Microscale wear of vitrified abrasive materials. J Mater Sci 39:2131–2143

28. Marinescu ID, Rowe WB, Dimitrov B, Inasaki I (2004) Tribology of abrasive machining processes. William Andrew, Inc., Norwich

29. Wang J, Scott W, Zhang L (1999) Abrasive technology: current development and applications I. World Scientific Publishing Co., Singapore

30. Nadolny K (2011) Durability of Al$_2$O$_3$ grinding wheels with zone-diversified structure in single-pass internal cylindrical grinding. Adv Manuf Sci Technol 35(3):39–53

31. Nadolny K, Słowinski B (2011) The effects of wear upon the axial profile of a grinding wheel in the construction of innovative grinding wheels for internal cylindrical grinding. Adv Tribol. doi:10.1155/2011/516202

32. Nadolny K (2009) Device for shaping conical chamfer on the grinding wheel surface for small angular values. Polish patent No. P.215803

33. Nadolny K, Kaplonek W (2012) Design of a device for precision shaping of the grinding wheel macro- and microgeometry. J Cent South Univ T 19(1):135–143

34. Klocke F, Engelhorn R, Mayer J, Weirich T (2002) Micro-analysis of the contact zone of tribologically loaded second-phase reinforced sol-gel-abrasives. CIRP Ann 51(1):245–250

35. Mayer J, Engelhorn R, Bot R, Weirich T, Herwartz C, Klocke F (2006) Wear characteristics of second-phase-reinforced sol-gel corundum abrasives. Acta Mater 54(13):3605–3615

36. Evans AG (1979) Science of ceramic machining and surface finishing II. Washington (DC). US Government Printing Office 1-14

37. Steijn RP (1961) On the wear of sapphire. J Appl Phys 32(10):1951–1959

38. Duwell EJ (1962) Friction and wear of single-crystal sapphire sliding on steel. J Appl Phys 33(9):2691–2699

39. Cannon RM, Rhodes WH, Heuer AH (1980) Plastic deformation of fine-grained alumina (Al$_2$O$_3$): I, interface-controlled diffusional creep. J Am Ceram Soc 63(1–2):46–53

40. Heuer AH, Tighe NJ, Cannon RM (1980) Plastic deformation of fine-grained alumina (Al$_2$O$_3$): II, basal slip and nonaccommodated grain-boundary sliding. J Am Ceram Soc 63(1–2):53–61

41. Krauss G (2005) Steels: processing, structure, and performance. ASM International

42. Smallman RE, Bishop RJ (1999) Modern physical metallurgy and materials engineering: science, process, applications. Butterworth-Heinemann, Oxford